



J. Serb. Chem. Soc. 91 (0) 1–14 (2026)
JSCS–13610

Hydrothermal synthesis of VO₂(B) and its phase transformation to VO₂(M): Investigating metal–insulator transition behavior

AISHWARYA RAJGONDA PATIL,¹ KRISHNA CHAITANYA SOLASA,¹ SOURAV KUMAR,² SHREEYA RANE³ and PALASH ROY CHOUDHURY^{4*}

¹*École Centrale School of Engineering, Mahindra University, Hyderabad, India,*

²*Department of Metallurgical Engineering and Materials Science, IIT Indore, India,*

³*Department of Physics, University of Warwick, UK and* ⁴*Mahindra University, Survey No: 62/1A, Bahadurpally, Jeedimetla, Hyderabad, Telangana 500043, India*

(Received 1 November, revised 16 December 2025, accepted 22 April 2026)

Abstract: In this study, VO₂(B) nanostructures were synthesized *via* a stabilizer-free hydrothermal route and successfully converted to VO₂(M) at 350 °C in just 30 min. This process offers a reduced thermal budget compared to established protocols, which generally require temperatures above 400 °C and durations exceeding 1 h. The resulting urchin-like VO₂ nanostructures were characterized using a variety of techniques such as XRD, Raman spectroscopy, SEM and DSC to investigate their structural evolution, surface morphology and metal–insulator transition characteristics. The experimental results reveal that VO₂(B) predominantly transforms to VO₂(M) upon annealing at 350 °C, with minor secondary oxide phases. Furthermore, the annealing at 450 °C led to the complete phase transformation of VO₂ to V₂O₅, indicating the sensitivity of VO₂ to annealing temperature. The results show that the insulator-to-metal transition temperature to be ~65 °C, which is lower than that of bulk VO₂ (~68 °C), indicating modified transition behavior in the nanostructured samples. These results demonstrate that hydrothermally synthesized VO₂(B) can be converted to predominantly VO₂(M) by annealing at 350 °C for 30 min, enabling the observation of a reversible metal–insulator transition near 65 °C.

Keywords: VO₂ nanostructures; hydrothermal synthesis; annealing effect; metal–insulator transition.

INTRODUCTION

Materials exhibiting a metal–insulator transition (MIT) are used in resistive random-access memory (ReRAM) for non-volatile storage of data. Often this transition accompanies a corresponding change in their crystal structure and symmetry.¹ A transition between crystalline and amorphous phases may be exploited

* Corresponding author. E-mail: palashroychoudhury@gmail.com
<https://doi.org/10.2298/JSC251101022P>

for use in next-generation non-volatile memory because this transition corresponds to different resistive states.² Such materials can mimic neural synapses, which is essential in neuromorphic computing where devices emulate the human brain.³ A gradual, analog variation in resistance near the MIT provides a means to model synaptic plasticity, achievable with materials that show progressive, voltage-dependent resistance changes.⁴ Materials with MIT also hold promise in electronics beyond memory applications. They have the ability to replace conventional transistors in field-effect transistors (FETs), potentially enhancing energy efficiency and making the way for ultra-low-power computing.⁵ The sharp MIT in materials like VO₂ at specific temperatures can be used in thermal switches for managing heat flow in electronics.⁶ These materials can act as thermal insulators below the transition temperature and as thermal conductors above it. A sharp MIT, which is associated with changes in crystal structure, may also exhibit changes in optical properties.⁷ This property may be exploited to construct optical sensors and smart windows that can automatically modulate light of a certain frequency. Oxides undergoing MIT without concurrent magnetic transitions are promising candidates for spin-based quantum applications, where control over electronic phases without perturbing spin order is advantageous.⁸ Some materials exhibit a high Seebeck coefficient near the MIT temperature that can be useful for thermoelectric applications.⁹ This could enable the development of efficient thermoelectric generators for waste heat recovery, enhancing energy efficiency across various industries.

Materials undergoing an MIT have attracted significant interest due to the abrupt, reversible modulation of their properties. Among these, vanadium dioxide (VO₂) is a premier candidate for next-generation smart windows, thermal switches, and energy-responsive devices. Interest in VO₂ is driven particularly due to its fully reversible structural and electronic transition occurring at a near-ambient temperature of approximately 68 °C.

Vanadium dioxide possesses many possible crystalline forms or polymorphs, some of which are stable, and others metastable. These include VO₂(M), VO₂(R), VO₂(A), VO₂(B), VO₂(C), VO₂(D) and VO₂ (paramontroseite).¹⁰ Out of these, the MIT is associated with the transition between the metallic VO₂(R) phase above 68 °C and the insulating VO₂(M) phase below 68 °C. Many techniques have been used for VO₂ synthesis, including the sol–gel method,¹¹ magnetron sputtering,¹² chemical vapor deposition¹³ and the hydrothermal method.^{10,14} Among these, the hydrothermal method is known to have minimal environmental impact and is often employed to synthesize the metastable VO₂(B) phase. Vanadium pentoxide and ammonium metavanadate (NH₄VO₃) are commonly used vanadium sources in the hydrothermal synthesis of VO₂. Commonly used reducing agents include oxalic acid,¹⁵ hydrazine hydrate,¹⁶ ethylene glycol,¹⁷ octadecyl amine,¹⁸ citric acid,¹⁶ formic acid¹⁹ and formaldehyde.²⁰ Out of these, oxalic acid has been the most preferred reductant in the hydrothermal synthesis of VO₂ due to its low toxicity

and ease of use. Zhu *et al.*¹⁵ reported the synthesis of several types of VO₂(B) nanostructures by a hydrothermal reaction combining (NH₄VO₃) and oxalic acid at different times and temperatures. The resulting products had combinations of nanorods, nanoflakes and nanoflowers with the concentration of oxalic acid influencing their proportions.¹⁵

In this paper, we report a simple method for the preparation of VO₂(M) *via* heat treatment of hydrothermally derived VO₂(B). The effect of different annealing conditions on the final products was characterized using X-ray diffraction (XRD), Raman spectroscopy, scanning electron microscopy (SEM) and UV–Vis spectroscopy, while the thermochemical properties were studied using differential scanning calorimetry (DSC).

EXPERIMENTAL

Synthesis of VO₂(B)

We synthesized VO₂(B) by a hydrothermal reaction between commercial vanadium pentoxide powder and oxalic acid. Firstly, 0.73 g of V₂O₅ (1 mmol) was added to a beaker containing 40 mL deionized water. This mixture was stirred under ambient conditions for 5 min using a magnetic stirrer. Then, 1.51 g of H₂C₂O₄·H₂O (3 mmol) was added to it and further stirred for 5 min, yielding a green solution indicating partial reduction. This solution was continuously stirred at 80 °C until the aqueous solution turned into a clear, transparent dark blue color. The change in color implied a reduction of vanadium from V⁵⁺ to V⁴⁺. Then, this solution was transferred into a Teflon[®]-lined stainless-steel autoclave, which was kept in a preheated oven (at 220 °C) for 3 h to complete the hydrothermal reaction for a duration of 3 h. The resulting bluish-black colored precipitate was separated by centrifugation. This precipitate was then washed with ethanol and DI water several times to remove any contamination and was dried for 12 h at 60 °C in an oven. This yielded black colored vanadium dioxide powder (henceforth referred to as S-22). The resulting powder was subsequently ground in a mortar and pestle and subjected to annealing in a tube-furnace at various temperatures. Fig. 1 illustrates the various steps involved in the synthesis of vanadium oxide nanobelts.

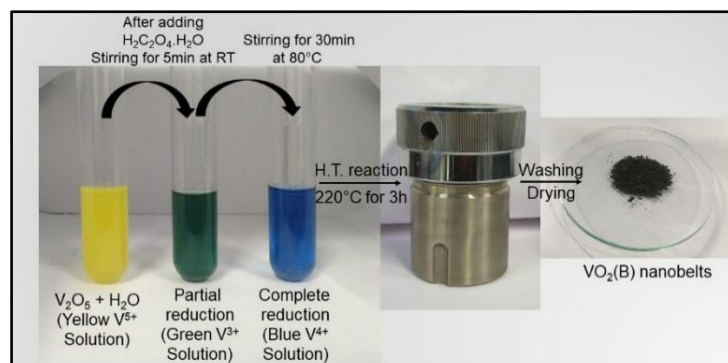


Fig. 1. Schematic illustration of the entire reaction mechanism during hydrothermal synthesis of VO₂ nanobelts.

Synthesis of VO₂(M)

VO₂(M) was derived from VO₂(B) through a controlled annealing process. A 500 mg sample from the as-synthesized VO₂ (S-22) was taken and annealed at different temperatures, namely 300, 350, 400 and 450 °C (henceforth addressed as S-30, S-35, S-40 and S-45, respectively) for 30 min in a quartz-tube vacuum furnace under low vacuum (10⁻² mbar). Both the heating and cooling rates were maintained at 5 °C/min.

Characterization

The crystal structure of the powder samples was characterized by XRD (Rigaku-D/MAX-RB) with CuK α radiation ($\lambda = 0.154$ nm). The data were analyzed using SMARTLab software. The samples were scanned over a 2θ range of 15–60°. Additionally, chemical and phase analysis were performed using a Raman spectrometer (Horiba, LabRAM) with a 633 nm laser excitation source. The microstructure and surface morphology of the sample were examined using field-emission SEM (FE-SEM, Jeol). Differential scanning calorimetry (DSC, TA Instruments, model 2910) studies were performed to investigate phase transition behavior over a temperature range of 15–100 °C using heating and cooling rates of 10 °C/min. Optical transmittance measurements were carried out using a UV-Vis spectrometer (Ocean Insights) in the wavelength range of 200–800 nm to evaluate the optical properties of the material.

RESULTS AND DISCUSSION

Structural studies

The crystalline phase and purity of the precursor, as-prepared and annealed samples were determined by XRD and obtained results are shown in Fig. 2. The V₂O₅ spectrum is that of the precursor used for synthesis. The XRD patterns are readily assigned to V₂O₅ (ICDD: 09-0387), which reveals the purity of the precursor. S-22 shows peaks that are in close agreement with the VO₂(B) phase with Miller indices (*hkl* planes) indicating growth of the monoclinic VO₂(B) phase (ICDD: 01-84-7141). The lattice parameter values calculated are as follows: $a = 12.04$ Å, $b = 3.68$ Å and $c = 6.43$ Å and it shows *C2/m* space group symmetry, with the strongest peaks at 2θ 25.28, 29.09, 30.13, 37.01, 49.28 and 55.24° corresponding to (110), (002), (111), (202), (11 $\bar{3}$) and (221) planes, respectively. Additionally, VO₂(B) also exhibits a high degree of crystallinity, evidenced by the well-defined and strong XRD peaks. The diffraction peak at 2θ 42.2° is indexed to the VO₂(M) phase (ICDD: 01-076-0456) for the (21 $\bar{2}$) plane. There is no evidence of diffraction peaks corresponding to secondary oxide phases, such as V₂O₅. These results confirm that the VO₂(B) phase is predominant, with no secondary oxides detected within XRD resolution limits. S-30 remains predominantly VO₂(B), with trace reflections indicating the onset of the phase transition to VO₂(M).

From the analysis of the XRD data, we observe that annealing the sample S-35 at 350 °C resulted in the formation of a predominantly monoclinic VO₂(M) phase, with minor secondary phases of V₂O₅ and V₃O₇. The lattice constants are $a = 5.75$ Å, $b = 4.54$ Å and $c = 5.38$ Å, indicating a monoclinic structure with *P2₁/c* space group symmetry. The peaks detected at 2θ 27.79, 37.01, 39.72, 42.20, 51.24, 55.45

and 57.33° are assigned to the (001), (21 $\bar{1}$), (020), (21 $\bar{2}$), (22 $\bar{1}$), (220) and (022) planes, respectively, for the monoclinic VO₂(M) phase (ICDD: 01-076-0456).

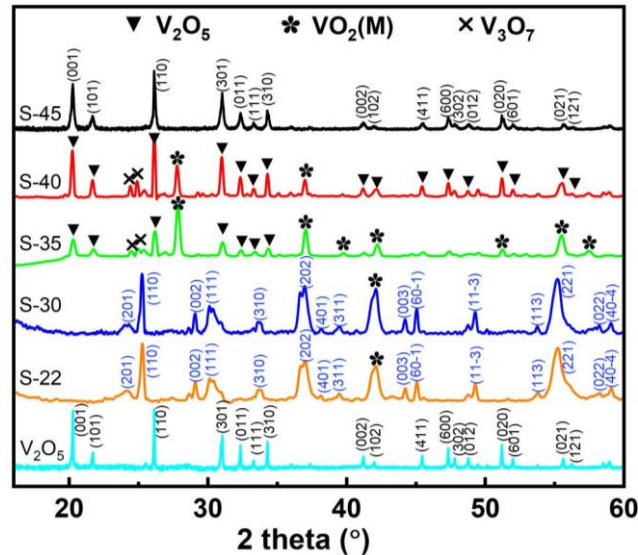


Fig. 2. XRD patterns of pristine V₂O₅, the hydrothermally synthesized sample (S-22) and samples annealed at various temperatures (S-30, S-35, S-40 and S-45) for 30 min.

The XRD patterns of sample S-40 are a combination of phases with the presence of both VO₂(M) and peaks belonging to V₂O₅ and V₃O₇ (ICDD: 042-0876). It can be noted that with the increase in annealing temperature, the intensities of the peaks of VO₂(M) decrease while the intensities of the V₂O₅ peaks increase, showing reduced thermal stability of the VO₂ phase at elevated temperatures. In contrast, the XRD spectra of S-45 show complete oxidation of VO₂ to V₂O₅, which agrees well with existing literature.^{21,22} This indicates that during high-temperature treatment, metastable VO₂ may have oxidized and transformed into its most thermodynamically stable phase, V₂O₅ (ICDD: 09-0387), which is the same as the precursor used for VO₂ synthesis. The average crystallite sizes estimated using Scherrer's formula for samples S-22, S-30, S-35, S-40 and S-45 are 19, 22, 24, 31 and 31 nm, respectively.

Raman spectroscopy was used to analyze the structural and phase information in addition to XRD. Raman spectra of S-22, the precursor V₂O₅ and the annealed samples are shown in Fig. 3a and b. Characteristic peaks at 146 and 197 cm⁻¹ are consistent with orthorhombic V₂O₅, indicating high purity and crystallinity of the precursor. The Raman modes at 285 and 406 cm⁻¹ correspond to the bending modes of V=O bonds, and the one at 482 cm⁻¹ is attributed to the bending of

V–O–V bonds. The peaks at 528 and 701 cm^{-1} are attributed to V–O bonds (combined stretching and bending vibrations). The 995 cm^{-1} peak arises from the stretching of the V=O bond.^{23–25}

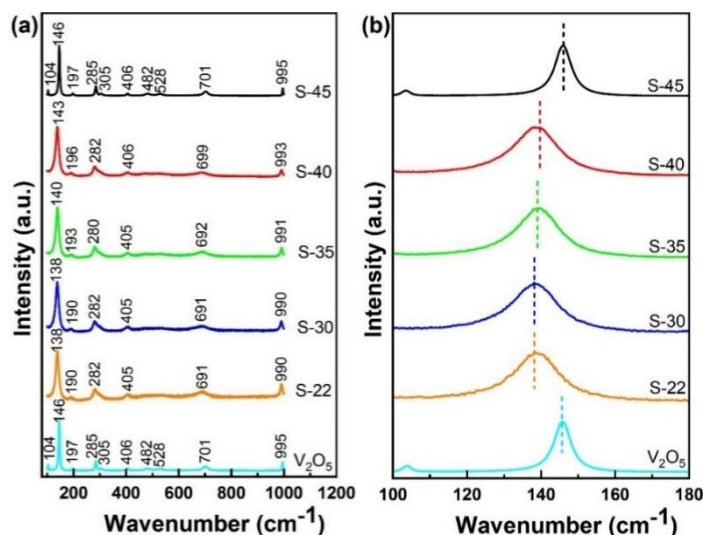


Fig. 3. Raman spectra of all samples: a) full spectra and b) Raman spectra in the range of 135–150 cm^{-1} highlighting the peak shift.

Furthermore, the Raman spectrum of the hydrothermally synthesized VO₂(B) phase (S-22) exhibits broad peaks at 138, 190, 282, 405, 691 and 990 cm^{-1} . The peaks at 138 and 282 cm^{-1} are attributed to V–O–V bending vibrations, while the 405 cm^{-1} peak corresponds to V–O–V stretching. The band at 691 cm^{-1} is associated with the coordination of three oxygen atoms around a vanadium center, and the strong peak at 990 cm^{-1} arises from V=O stretching vibrations. According to Cheng *et al.*²⁶ and Zhang *et al.*,²⁷ the above Raman peaks can be indexed to vibrational bands of the VO₂(B) phase.

The sample S-30 exhibits characteristics similar to VO₂(B), indicating the stability of the phase up to this temperature. For the samples S-35 and S-40, we observe a shift in peaks to higher frequencies (140, 280 and 692 cm^{-1}), indicating the formation of mixed phases and partial oxidation of VO₂(M). Finally, for the sample S-45, the Raman spectrum exhibits sharp peaks identical to those of the original V₂O₅ precursor, indicating complete oxidation. The zoomed region between 135–150 cm^{-1} (Fig. 3b) provides insights into peak shifts and the phase transition from VO₂(B) to VO₂(M). Thus, the development of the Raman bands corresponds well with the structural changes established using XRD and demonstrates the sensitivity of Raman spectroscopy for characterizing the long-range order and local structural changes.

A detailed analysis of the Raman spectra for samples S-35 and S-40, which consist of mixed phases of VO₂(M) and V₂O₅, indicates that these phases cannot be distinctly resolved *via* Raman spectroscopy due to the overlap in their characteristic vibrational modes. Thus, phase identification in this case needs to be done from X-ray diffraction (XRD) data. Additionally, the Raman spectrum of sample S-45 exhibits features consistent with V₂O₅, indicating a phase transformation from VO₂ to V₂O₅, and closely matches the spectral signature of the V₂O₅ precursor. Raman spectroscopy thus serves as a complementary technique to XRD, confirming that our simple synthesis method reliably produces VO₂ with MIT behavior.

Morphological studies

The morphology of VO₂ nanostructures was analyzed using SEM. Fig. 4 shows the SEM images of the as-grown and annealed vanadium oxide nanostructures. For the samples S-22, shown in Fig. 4a, multiple nanobelts are connected at the bottom and spread radially towards the top to form an urchin-like unit.

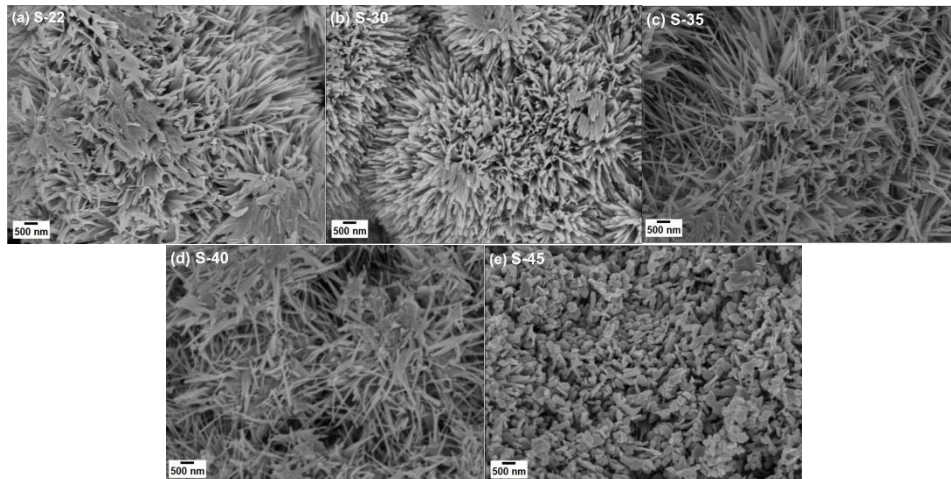


Fig. 4. SEM images illustrating the morphology of the nanostructure samples: a) S-22, b) S-30, c) S-35, d) S-40 and e) S-45.

The width of the nanobelts in the as-grown samples varies from ~50 to ~150 nm, and their length is in the sub-micrometer range. These urchin-like structures are symmetric with diameters ranging between 5–15 μm . This initial morphology is altered in the annealed samples. From the SEM image of S-30, we observe sharper needle-like structures compared to S-22, indicating denser, well-connected features with morphology that is consistent with the phase evolution observed from XRD data. The micrographs of samples S-35 and S-40 show a somewhat mixed microstructure. The micrograph of sample S-45 shows a significant change, where

needle-like features disappear, and the surface appears to develop granular features. Here, we did not detect the existence of the $\text{VO}_2(\text{M})$ phase and instead observe the formation of pure V_2O_5 . In summary, SEM analysis demonstrates that annealing temperatures strongly influence the morphological evolution of the nanostructures, while the associated changes in crystallinity and phase composition are confirmed by XRD data.

Optical properties

We performed UV–Vis spectroscopy to study the transmittance characteristics of vanadium oxide nanostructures. We calculated the optical band gap of these nanostructures with the help of a Tauc plot, which follows the equation:

$$\alpha h\nu = A(h\nu - E_g)^n \quad (1)$$

Where E_g is the band gap, α is the absorption coefficient, $h\nu$ represents the energy of light, A is a constant and n denotes the nature of the transition.

Fig. 5 illustrates the effect of various annealing temperatures on the optical characteristics of the samples. The UV–Vis transmission spectra (Fig. 5a) indicate that the transmittance generally increases with annealing temperature, indicating improved crystallinity in the samples.

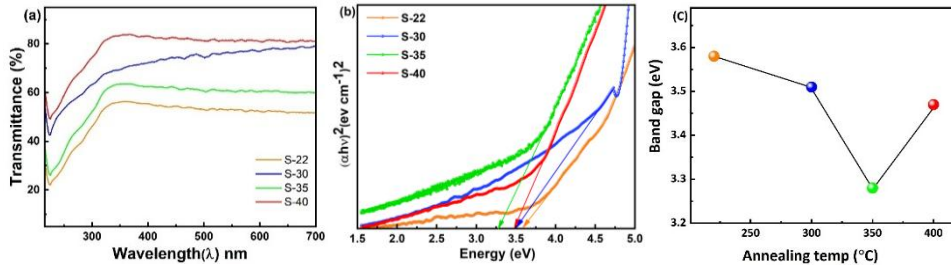


Fig. 5. a) Optical transmittance spectra of the samples annealed at various temperatures; b) corresponding Tauc plots representing the magnitude of the direct optical band gap; c) changes in optical band gap values with annealing temperature.

We calculated the direct band gap energies, from the Tauc plots in Fig. 5b, by extrapolating $(ah\nu)^2$ versus energy ($h\nu$). The plots reveal a distinct trend of decreasing in optical band gap values with increasing annealing temperature up to 350 °C. Following this, there was a modest increase of the band gap at 400 °C. Corresponding band gap values were calculated from the Tauc plots. As shown in Fig. 5c, E_g decreases from 3.6 eV for sample S-22 to a minimum of 3.3 eV for sample S-35 and subsequently increases to 3.5 eV for sample S-40. Despite the minor morphological variations, the changes in E_g are primarily governed by phase transitions, as observed through XRD analysis. The increased band gap in hydro-

thermally synthesized urchin-like VO₂ samples with respect to bulk VO₂^{28,29} (typically 0.6–0.7 eV for the monoclinic structure) can be explained by several factors. Nanoscale crystallite size leads to quantum confinement effects, producing a wider band gap. Since VO₂(B) was found to have a wider band gap than VO₂(M), the existence of both monoclinic (M) and metastable B phases together also contributes to the wider band gap.³⁰ The lattice distortion and structural distortions also change the electronic structure. Defects and oxygen vacancies create localized states that change the band gap.³² All these factors together are the potential reasons behind the much broader band gap in the VO₂ nanostructures.

Thermochromic properties

Fig. 6 presents the differential scanning calorimetry (DSC) thermograms of VO₂(B) powders annealed at various temperatures (300–450 °C) for 30 min, with corresponding thermal parameters summarized in Table I. The transition temperature (T_C) was determined as the midpoint between the endothermic peak temperature during heating and the exothermic peak temperature during cooling. Samples S-22, S-30 and S-45 do not display any prominent endothermic or exothermic peaks in the DSC curves. The absence of a clear metal–insulator transition in S-22 and S-30 can be attributed to the dominance of the VO₂(B) phase, which does not exhibit a sharp transition like monoclinic VO₂(M). In addition, broader XRD peaks were observed for these samples, indicating reduced crystallinity. This leads to weaker cooperative lattice distortion, which is necessary for an abrupt structural transition. For sample S-45, the disappearance of the transition is due to the dominant V₂O₅ phase as identified by XRD, which does not exhibit a metal–insulator transition in this temperature range.^{31,32}

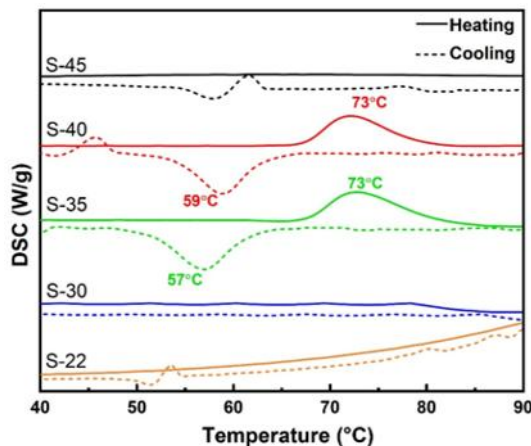


Fig. 6. DSC results illustrating a well-defined, reversible metal–insulator transition exclusively in the specimens annealed at 350 and 400 °C. In contrast, other samples exhibit a featureless thermal profile indicating the absence of a detectable phase transition.

For the samples S-35 and S-40, the endothermic peak maximum during the heating cycle remains nearly constant at ~ 73 °C. However, the exothermic peak

during the cooling cycle shifts slightly from 57 °C for S-35 to 59 °C for S-40. As a result, the calculated transition temperature (T_C , determined as the midpoint between heating and cooling peaks) increases only slightly from 65 °C (for S-35) to 66 °C (for S-40). Simultaneously, the thermal hysteresis width (ΔT), calculated as the difference between the heating and cooling transition temperatures, decreases from 16 to 14 °C. A reduction in the magnitude of ΔT suggests improved reversibility of the structural transformation. This behavior correlates with the enhanced crystallinity observed in the XRD patterns of S-40 relative to S-35, implying that improved structural ordering contributes to a more uniform and coherent phase transition. The observed T_C values are slightly lower than those of bulk $\text{VO}_2(\text{M})$, which is typically ~ 68 °C. This reduction to ~ 65 °C can be attributed to residual $\text{VO}_2(\text{B})$ and nanocrystalline interfaces. Overall, the appearance and sharpness of the metal–insulator transition are strongly governed by phase composition and crystallinity. Samples dominated by $\text{VO}_2(\text{B})$ or V_2O_5 do not exhibit a prominent transition, whereas samples containing predominantly the monoclinic $\text{VO}_2(\text{M})$ phase exhibit a distinct and reversible MIT. The improved crystallinity observed in XRD for S-35 and S-40 contributes to a narrower hysteresis width and more consistent structural transformation. Similar reductions in transition temperature and broadening of the MIT in nanocrystalline or mixed-phase VO_2 systems have been reported in previous studies, where strain effects and phase heterogeneity were found to influence MIT behavior.^{33–35}

TABLE I. Comparison of phase transition temperatures obtained from DSC analysis during heating and cooling cycles

Sample	Annealing temp. °C	Dominant phase	Secondary phase	T_{heat} °C	T_{Cool} °C	T_C °C	ΔT °C
S-22	As-synthesized	$\text{VO}_2(\text{B})$	–	–	–	–	–
S-30	300	$\text{VO}_2(\text{B})$	$\text{VO}_2(\text{M})$	–	–	–	–
S-35	350	$\text{VO}_2(\text{M})$	V_2O_5 , V_3O_7	73	57	65	16
S-40	400	V_2O_5	$\text{VO}_2(\text{M})$, V_3O_7	73	59	66	14
S-45	450	V_2O_5	–	–	–	–	–

The reduction in hysteresis width may be attributed to partial conversion of $\text{VO}_2(\text{B})$ to V_2O_5 , as detected by X-ray diffraction (XRD). It may also be due to the presence of defects at the interface.³⁴ In contrast, samples S-35 and S-40 clearly exhibit a phase transition, consistent with the phase evolution confirmed by XRD.

In addition, sample S-35 exhibited an average transmittance of up to about 59 % obtained at room temperature (300 K), which is comparable to or slightly improved compared to published literature.^{32,33} Phase transformation in VO_2 was clearly observed for samples annealed at 350 °C, demonstrating that this procedure is simple and energy efficient. For an observable phase transition in VO_2 prepared by reduction of V_2O_5 , the required annealing temperature is often above 400 °C

and the annealing time is more than 1 h as reported in previous works.^{36,37} Our method lowers the thermal budget by achieving VO₂ phase transformation faster (30 min) and at a lower annealing temperature than previously reported schemes. The resulting VO₂(M) nanostructures exhibit reversible thermochromic behavior.

Integrating XRD, Raman, optical and DSC analyses indicates a distinct phase–property correlation across the synthesized and annealed nanostructures. Specimens dominated by VO₂(B) (S-22, S-30) are characterized by broadened diffraction profiles and wider band gaps, while also lacking an observable MIT. In contrast, the formation of a predominantly VO₂(M) phase at 350 °C (S-35) is associated with significant band gap narrowing and the emergence of a well-defined, reversible MIT near 65 °C. Progressive oxidation from 400–450 °C results in the formation of V₂O₅, which effectively suppresses this transition. These findings show that phase purity and crystallinity are major factors governing the thermochromic properties and MIT in these nanostructures.

CONCLUSION

VO₂ nanostructures were synthesized using a stabilizer-free hydrothermal process followed by controlled thermal annealing. The as-prepared sample (S-22) predominantly exhibited the metastable VO₂(B) phase with high crystallinity. Annealing at 350 °C resulted in the formation of a predominantly monoclinic VO₂(M) phase, accompanied by minor secondary phases of V₂O₅ and V₃O₇. With a further increase in annealing temperature to 400 °C, V₂O₅ became the predominant phase while the relative intensity of VO₂(M) decreased, indicating progressive oxidation of VO₂. Annealing at 450 °C resulted in the complete oxidation of VO₂ to V₂O₅. While the crystallite size increased with annealing temperature, the band gaps exhibited a non-monotonic variation with annealing temperature and phase composition. The sample annealed at 350 °C showed an average room-temperature transmittance of 59 % and a phase-transition temperature of ~65 °C. Samples S-35 and S-40 exhibit clear, reversible phase transitions between 65 and 66 °C. In summary, we demonstrate the tunability of phase composition and transition behavior in annealed VO₂ nanostructures and provide insight into the relationship between structural evolution and metal–insulator transition behavior. Our demonstration of a cost-effective and stabilizer-free hydrothermal synthesis route also offers a reduced thermal budget route for scalable vanadium dioxide production, enabling controlled phase evolution and metal–insulator transition behavior in VO₂ nanostructures.

Acknowledgements. The authors want to acknowledge the support and facilities provided by National Institute of Technology Raipur, India. The author also wants to acknowledge the Guru Ghasidas University Bilaspur, India for granting the study leave to do Ph.D.

ИЗВОД

ХИДРОТЕРМАЛНА СИНТЕЗА И ФАЗНА ТРАНСФОРМАЦИЈА VO₂(B) У VO₂(M):
ИСТРАЖИВАЊЕ ПРЕЛАЗА МЕТАЛ–ИЗОЛАТОРAISHWARYA RAJGONDA PATIL,¹ KRISHNA CHAITANYA SOLASA,¹ SOURAV KUMAR,² SHREEYA RANE³
И PALASH ROY CHOUDHURY⁴¹*École Centrale School of Engineering, Mahindra University, Hyderabad, India,* ²*Department of Metallurgical Engineering and materials science, IIT Indore, India,* ³*Department of Physics, University of Warwick, UK и* ⁴*Mahindra University, Survey No: 62/1A, Bahadurpally, Jeedimetla, Hyderabad, Telangana 500043, India*

У овом раду, VO₂(B) наноструктуре су синтетизоване хидротермалним путем без стабилизатора и успешно конвертоване у VO₂(M) на 350 °C за само 30 min. Овим поступком се постиже уштеда енергије у односу на уобичајене поступке, који генерално захтевају температуре више од 400 °C и трајање дуже од једног сата. Добијене VO₂ наноструктуре са игличастим честицама су окарактерисане коришћењем различитих техника као што су XRD, раманска спектроскопија, SEM и DSC како би се испитао фазни састав, морфологија и карактеристике прелаза метал-изолатор. Експериментални резултати показују да се VO₂(B) претежно трансформише у VO₂(M) након калцинације на 350 °C, са малим уделом секундарних оксидних фаза. Додатно, жарење на 450 °C довело је до потпуне фазне трансформације VO₂ у V₂O₅, што указује на осетљивост VO₂ на температуру калцинације. Температура прелаза изолатор-метал је ~65 °C, што је ниже него за VO₂ у комаду (~68 °C), што указује на модификовано понашање прелаза у наноструктурним узорцима. Ови резултати показују да се хидротермално синтетисани VO₂(B) може трансформисати претежно у VO₂(M) жарењем на 350 °C током 30 min, што омогућава реверзибилни прелаз метал–изолатор близу 65 °C.

(Примљено 1. новембра, ревидирано 16. децембра 2025, прихваћено 22. априла 2026)

REFERENCES

1. A. B. Georgescu, A. J. Millis, *Commun. Phys.* **5** (2022) 135 (<https://doi.org/10.1038/s42005-022-00909-z>)
2. A. Moatti, R. Sachan, J. Narayan, *J. Appl. Phys.* **128** (2020) 045302 (<https://doi.org/10.1063/5.0006671>)
3. G. Ekinici, B. Özkal, S. Kazan, *ACS Omega* **9** (2024) 26235 (<https://doi.org/10.1021/acsomega.4c02001>)
4. A. R. Galloni, Y. Yuan, M. Zhu, H. Yu, R. S. Bisht, C.-T. M. Wu, C. Grienberger, S. Ramanathan, A. D. Milstein, *Proc. Natl. Acad. Sci.* **121** (2024) e2318362121 (<https://doi.org/10.1073/pnas.2318362121>)
5. N. Shukla, A. V Thathachary, A. Agrawal, H. Paik, A. Aziz, D. G. Schlom, S. K. Gupta, R. Engel-Herbert, S. Datta, *Nat. Commun.* **6** (2015) 7812 (<https://doi.org/10.1038/ncomms8812>)
6. S. Jessadaluk, N. Khemasiri, P. Rattanawarinchai, S. Rahong, A. Rangkasikorn, N. Kayunkid, S. Wirunchit, A. Klamchuen, J. Nukeaw, *Jpn. J. Appl. Phys.* **58** (2019) SDDE12 (<https://doi.org/10.7567/1347-4065/ab0aca>)
7. A. Ainabayev, B. Walls, D. Casey, D. Caffrey, D. Mullarkey, A. McGlinchey, A. Khare, A. Tikhonov, C. Ilhan, D. Brennan, S. J. McCormack, I. Shvets, *J. Phys. Chem., C* **127** (2023) 24432 (<https://doi.org/10.1021/acs.jpcc.3c06057>)
8. R. Zhang, Q. S. Fu, C. Y. Yin, C. L. Li, X. H. Chen, G. Y. Qian, C. L. Lu, S. L. Yuan, X. J. Zhao, H. Z. Tao, *Sci. Rep.* **8** (2018) 17093 (<https://doi.org/10.1038/s41598-018-35490-5>)

9. Q. Song, J. Zhou, L. Meroueh, D. Broido, Z. Ren, G. Chen, *Appl. Phys. Lett.* **109** (2016) 263902 (<https://doi.org/10.1063/1.4973292>)
10. M. Li, S. Magdassi, Y. Gao, Y. Long, *Small* **13** (2017) 1701147 (<https://doi.org/10.1002/sml.201701147>)
11. M. M. Seyfour, R. Binions, *Solar Energy Mater. Solar Cells* **159** (2017) 52 (<https://doi.org/10.1016/j.solmat.2016.08.035>)
12. F. Xu, X. Cao, Z. Shao, G. Sun, S. Long, T. Chang, H. Luo, P. Jin, *ACS Appl. Mater. Interfaces* **11** (2019) 4712 (<https://doi.org/10.1021/acsami.8b20794>)
13. D. Malarde, M. J. Powell, R. Quesada-Cabrera, R. L. Wilson, C. J. Carmalt, G. Sankar, I. P. Parkin, R. G. Palgrave, *ACS Omega* **2** (2017) 1040 (<https://doi.org/10.1021/acsomega.7b00042>)
14. C. Wang, H. Xu, C. Wang, T. Liu, S. Yang, Y. Nie, X. Guo, X. Ma, X. Jiang, *J. Alloys Compd.* **877** (2021) 159888 (<https://doi.org/10.1016/j.jallcom.2021.159888>)
15. J. Ni, W. Jiang, K. Yu, Y. Gao, Z. Zhu, *Electrochim. Acta* **56** (2011) 2122 (<https://doi.org/10.1016/j.electacta.2010.11.093>)
16. S. R. Popuri, M. Miclau, A. Artemenko, C. Labrugere, A. Villesuzanne, M. Pollet, *Inorg. Chem.* **52** (2013) 4780 (<https://doi.org/10.1021/ic301201k>)
17. S. Zhang, Y. Li, C. Wu, F. Zheng, Y. Xie, *J. Phys. Chem., C* **113** (2009) 15058 (<https://doi.org/10.1021/jp903312h>)
18. B.-R. Jia, M.-L. Qin, Z.-L. Zhang, S.-M. Li, X.-L. Wang, M. Huang, H.-Y. Wu, Z. Chen, X. Lu, L. Zhang, X.-H. Qu, *J. Alloys Compd.* **704** (2017) 79 (<https://doi.org/10.1016/j.jallcom.2017.02.046>)
19. J. Liu, Q. Li, T. Wang, D. Yu, Y. Li, *Angew. Chem. Int. Ed.* **43** (2004) 5048 (<https://doi.org/10.1002/anie.200460104>)
20. K.-C. Zhou, D.-M. Cao, Z.-Y. Li, *Trans. Nonferrous Met. Soc. China* **16** (2006) 517 ([https://doi.org/10.1016/S1003-6326\(06\)60090-3](https://doi.org/10.1016/S1003-6326(06)60090-3))
21. H. H. Afify, S. A. Hassan, M. Obaida, A. Abouelsayed, *Phys., E* **114** (2019) 113610 (<https://doi.org/10.1016/j.physe.2019.113610>)
22. D. Alie, L. Gedvilas, Z. Wang, R. Tenent, C. Engtrakul, Y. Yan, S. E. Shaheen, A. C. Dillon, C. Ban, *J. Solid State Chem.* **212** (2014) 237 (<https://doi.org/10.1016/j.jssc.2013.10.023>)
23. M. Dhananjaya, N. G. Prakash, A. L. Narayana, O. M. Hussain, *Appl. Phys., A* **124** (2018) 185 (<https://doi.org/10.1007/s00339-017-1522-0>)
24. D. Dreifus, M. P. F. Godoy, A. C. Rabelo, A. D. Rodrigues, Y. G. Gobato, P. C. Camargo, E. C. Pereira, A. J. A. De Oliveira, *J. Phys., D* **48** (2015) 445002 (<https://doi.org/10.1088/0022-3727/48/4/445002>)
25. D. Surya Bhaskaram, R. Cheruku, G. Govindaraj, *J. Mater. Sci. Mater. Electron.* **27** (2016) 10855 (<https://doi.org/10.1007/s10854-016-5194-x>)
26. B. Cheng, H. Zhang, Q. Li, J. Liu, B. Liu, *Inorganics* **10** (2022) 122 (<https://doi.org/10.3390/inorganics10080122>)
27. S. Zhang, Z. Zou, T. Lv, S. Li, Y. Zhang, *Int. J. Electrochem. Sci.* **15** (2020) 7203 (<https://doi.org/10.20964/2020.08.05>)
28. H. W. Verleur, A. S. Barker, C. N. Berglund, *Rev. Mod. Phys.* **40** (1968) 737 (<https://doi.org/10.1103/RevModPhys.40.737>)
29. K. Schneider, *J. Mater. Sci. Mater. Electron.* **31** (2020) 10478 (<https://doi.org/10.1007/s10854-020-03596-0>)

30. Meenu, P. Kumar, B. S. Dehiya, *J. Nanosci. Technol.* **5** (2019) 584 (<https://doi.org/10.30799/jnst.195.19050102>)
31. F. Mehmood, R. Pachter, N. R. Murphy, W. E. Johnson, C. V. Ramana, *J. Appl. Phys.* **120** (2016) 191 (<https://doi.org/10.1063/1.4972038>)
32. F. Arteaga-Cardona, A. P. Franco-Bacca, F. Cervantes-Alvarez, J. J. Alvarado-Gil, N. R. Silva-González, U. Salazar-Kuri, *Appl. Phys., A* **127** (2021) 159 (<https://doi.org/10.1007/s00339-021-04309-y>)
33. C. Xu, G. Liu, M. Li, K. Li, Y. Luo, Y. Long, G. Li, *Mater. Des.* **187** (2020) 108396 (<https://doi.org/10.1016/j.matdes.2019.108396>)
34. K. L. Gurunatha, S. Sathasivam, J. Li, M. Portnoi, I. P. Parkin, I. Papakonstantinou, *Adv. Funct. Mater.* **30** (2020) 27 (<https://doi.org/10.1002/adfm.202005311>)
35. L. Liu, F. Cao, T. Yao, Y. Xu, M. Zhou, B. Qu, B. Pan, C. Wu, S. Wei, Y. Xie, *New J. Chem.* **36** (2012) 619 (<https://doi.org/10.1039/C1NJ20798A>)
36. B. S. Beckerle, A. B. Cezar, I. T. Neckel, W. H. Schreiner, A. G. Bezerra Jr., I. L. Graff, J. Varalda, D. H. Mosca, *J. Appl. Phys.* **134** (2023) 123 (<https://doi.org/10.1063/5.0169279>)
37. S. A. Corr, M. Grossman, Y. Shi, K. R. Heier, G. D. Stucky, R. Seshadri, *J. Mater. Chem.* **19** (2009) 4362 (<https://doi.org/10.1039/B900982E>).